Nanoscale

PAPER

View Article Online
View Journal | View Issue

Cite this: *Nanoscale*, 2015, **7**, 5311

Ultraviolet photodetectors with high photosensitivity based on type-II ZnS/SnO_2 core/shell heterostructured ribbons†

Xing Huang,[a,b] Yong-Qiang Yu,[c] Jing Xia,[a] Hua Fan,[a] Lei Wang,[a] Marc-Georg Willinger,*[b] Xiao-Ping Yang,[a] Yang Jiang,[c] Tie-Rui Zhang[a] and Xiang-Min Meng*[a]

Semiconducting heterostructures with type-II band structure have attracted much attention due to their novel physical properties and wide applications in optoelectronics. Herein, we report, for the first time, a controlled synthesis of type-II ZnS/SnO_2 heterostructured ribbon composed of SnO_2 nanoparticles that uniformly cover the surface of ZnS ribbon *via* a simple and versatile thermal evaporation approach. Structural analysis indicated that the majority of SnO_2 nanoparticles have an equivalent zone axis, *i.e.*, <–313> of rutile SnO_2, which is perpendicular to ±(2–1–10) facets (top/down surfaces) of ZnS ribbon. For those SnO_2 nanoparticles decorated on ±(01–10) facets (side surfaces) of ZnS ribbon, an epitaxial relationship of $(01–10)_{ZnO}//(020)_{SnO_2}$ and $[2–1–10]_{ZnO}//[001]_{SnO_2}$ was identified. To explore their electronic and optoelectronic properties, we constructed field-effect transistors from as-prepared new heterostructures, which exhibited an n-type characteristic with an on/off ratio of ~10^3 and a fast carrier mobility of ~33.2 $cm^2\ V^{-1}\ s^{-1}$. Owing to the spatial separation of photogenerated electron–hole pairs from type-II band alignment together with the good contacts between electrodes and ribbon, the resultant photodetector showed excellent photoresponse properties, including large photocurrent, high sensitivity (external quantum efficiency as high as ~2.4×10^7%), good stability and reproducibility, and relatively fast response speed. Our results suggest great potential of ZnS/SnO_2 heterostructures for efficient UV light sensing, and, more importantly, signify the advantages of type-II semiconducting heterostructures for construction of high-performance nano-photodetectors.

Received 8th January 2015,
Accepted 11th February 2015

DOI: 10.1039/c5nr00150a

www.rsc.org/nanoscale

1. Introduction

One-dimensional (1D) semiconducting heterostructures, serving as important building blocks for assembly of electronics and optoelectronics, attract great research interest nowadays owing to their novel physical and chemical properties.[1–13] Compared to individual-component semiconductors, 1D semiconducting heterostructures have the capability of showing not only multifunctionalities but also some unique and markedly improved optical and optoelectronic properties, due to the combination of different functional components.[14–24] Particularly in the field of photodetector research, studies have indicated that devices constructed from 1D semiconducting heterostructures can exhibit excellent optoelectronic performances that are superior to those of individual constituents. For instance, Fang *et al.* synthesized a type of single-crystalline ZnS/ZnO biaxial nanobelts, and the optimized optoelectronic performances of devices fabricated with those biaxial nanobelts are much better than those of pure ZnS or ZnO in terms of higher external quantum efficiency and faster response speed.[16] Very recently, Tian *et al.* found that photodetectors from electrospun ZnO/SnO_2 fiber films can present high UV sensitivity and extremely large photo-dark current ratio, suggesting great potential of this material for efficient UV light sensing.[17] Therefore, development of heterostructured nanomaterials opens up new opportunities for fabrication of high-performance optoelectronics, which remains

[a]*Key Laboratory of Photochemical Conversion and Optoelectronic Materials, Technical Institute of Physics and Chemistry, Chinese Academy of Sciences, Beijing, 100190, P. R. China. E-mail: mengxiangmin@mail.ipc.ac.cn*
[b]*Department of Inorganic Chemistry, Fritz Haber Institute of the Max Planck Society, Faradayweg 4-6, 14195 Berlin, Germany. E-mail: willinger@fhi-berlin.mpg.de*
[c]*School of Electronic Science and Applied Physics, Hefei University of Technology, Hefei, 230009, P. R. China*

† Electronic supplementary information (ESI) available: SEM and TEM images of ZnS ribbons; EDX spectra of ZnS and ZnS/SnO_2 core/shell ribbon; HAADF-STEM image of ZnS/SnO_2 core/shell ribbon; Analysis of SAED pattern of ZnS/SnO_2 core/shell ribbon; HRTEM images of hetero-interface between ZnS and SnO_2 and relax atomic mode; HRTEM and relevant reconstructed IFFI-RGB images of the cross section ribbon; Schematic of the band alignment of ZnS/SnO_2 core/shell ribbon. Scheme S1. Schematic illustration of (a) the experimental setup and (b) the formation process of the ZnS/SnO_2 core/shell ribbon. See DOI: 10.1039/c5nr00150a

of extensive research interest and technically demanding in today's material science.

ZnS and SnO_2, with direct band-gaps of 3.77 eV and 3.6 eV respectively at room temperature, are important semiconductors and have been intensively investigated for a variety of electronic and optoelectronic applications.[25–35] With many efforts devoted in the past decade, significant progress has been made in their controlled synthesis and performance optimization for optoelectronic devices. However, due to their intrinsic physical and chemical characteristics, optoelectronic devices from those semiconductors often exhibit inherent problems in their use. For example, it has been demonstrated that individual ZnS nanostructure-based photodetectors generally suffer from low photocurrent and poor stability.[14,25,36] For photodetectors from SnO_2 nanostructures, their response speed and photocurrent stability are often unsatisfactory because of some natural defects, such as oxygen vacancies in the surface.[29,33,36] Alternatively, it is also worth mentioning that intrinsic ZnS-based photodetectors often show fast response speeds,[25] while photodetectors constructed from SnO_2 typically present large photocurrents, high sensitivity and good contact with electrodes.[37] One may expect that through combination of ZnS and SnO_2, the formed ZnS/SnO_2 heterostructure may integrate advantages from both individual components and exhibit optimized properties, such as large photocurrent, high stability and sensitivity, and relatively fast response speed. Additionally, it is known that ZnS/SnO_2 heterostructure has a type-II band alignment, in which both the conduction and the valence bands of the SnO_2 are lower in energy than those of the ZnS. The type-II band configuration of heterostructures has been demonstrated to be able to increase the lifetime of photogenerated electrons and holes efficiently by forming a charge separation state.[38,39] This feature could also be helpful for improving optoelectronic performance of the ZnS/SnO_2 heterostructure regarding its photocurrent, photosensitivity and so forth.

In this contribution, we show for the first time a rational design of type-II ZnS/SnO_2 core/shell ribbons *via* a simple two-step thermal evaporation method. The morphology, structure and composition of samples were systematically characterized by means of scanning electron microscopy (SEM), transmission electron microscopy (TEM) and energy-dispersive X-ray spectrometry (EDX), respectively. We show the first optoelectronic study of a photodetector assembled with the synthesized new ZnS/SnO_2 core/shell heterostructured ribbon. The device showed good optoelectronic performances, including large photocurrent, high photosensitivity, good stability, and so forth. Our result indicates that the ZnS/SnO_2 heterostructures could be of use for efficient UV-light sensing.

2. Experimental section

2.1. Synthesis of ZnS ribbons

ZnS ribbons were synthesized by a H_2 assisted thermal evaporation method in a high-temperature tube furnace with two heating zones. A high-purity commercial ZnS powder (analytical grade, 99.99%) was put in a ceramic boat and was loaded into the center of the heating zone. A silicon wafer coated with a layer of Au was placed downstream from the source about 5–7 cm away from it. After the system was pumped down to a pressure of 0.1 Pa, high-purity argon mixed with 5% hydrogen with a constant rate of 100 sccm (standard cubic centimeters per minute) was flowed into the tube. The pressure of the tube was maintained at about 4×10^4 Pa and the boat was heated at a rate of 30 °C min^{-1} to 1100 °C and maintained for 3 hours. After the system was cooled to room temperature, a white-colored product was found deposited on the silicon wafer.

2.2. Synthesis of ZnS/SnO_2 core/shell ribbons

In this synthesis, high-purity SnO powder was used as the source material and put at the centre of the high-temperature zone. The as-prepared ZnS ribbons on Si wafer acting as template were placed at the centre of the low-temperature zone. Then, high-purity argon mixed with 5% hydrogen with a constant rate of 45 sccm was flowed into the tube after pumping down to a pressure of 0.1 Pa. Then the SnO powder and the ZnS ribbon were heated to 850 °C and 600 °C respectively and kept for a duration of 1.5 hours. After the deposition, the furnace was naturally cooled down to room temperature and an off-white product was then obtained.

2.3. Preparation of cross-sectional ZnS/SnO_2 core/shell ribbons

The sectional ZnS/SnO_2 heterostructured ribbon nanotubes were firstly embedded in an epoxy plastic which was then cut into slices with a section of about 50–100 nm thick by a PowerTome ultramicrotome. Finally, those slices were transferred onto a Cu TEM grid for characterization.

2.4. Fabrication of nano-back-gate field-effect transistors (FETs) based on individual ZnS/SnO_2 core/shell ribbons

In this fabrication, ZnS/SnO_2 core/shell ribbons were firstly dispersed onto a SiO_2 (300 nm)/p^+-Si substrate, and then ITO (80 nm) electrodes, serving as the drain and source electrodes, were deposited on the ribbons by standard photolithography and lift-off processes using a pulsed laser deposition system with a KrF excimer laser (Lambda Physik COMPexPro 102, 248 nm, 150 mJ, 5 Hz). In addition, Au was utilized as the electrode material and was deposited on heterostructured ribbons by a high-vacuum electron-beam evaporation system, for comparison. Subsequently, a fast annealing process was performed on devices in Ar gas at 450 °C for 5 minutes to further improve the electrical contact between the electrodes and the ribbons.

2.5. Characterization and measurements

SEM images of the samples were obtained with a Hitachi S-4300 scanning electron microscope operated at 10 kV. X-ray diffraction patterns of the samples were recorded with a Bruker D8 Focus powder X-ray diffractometer using Cu-Kα radiation (λ = 1.5418 Å). TEM images, high-resolution TEM (HRTEM) images, selected area electron diffraction (SAED) pat-

terns and EDX mapping were recorded using an FEI aberration-corrected Titan 80–300 microscope operated at 300 kV equipped with an EDX detector. The electrical properties of the devices were tested by a semiconductor parameter analyzer system (Keithley 4200-SCS) at room temperature. To measure the photoresponse properties of core/shell ribbons, a monochromatic light source composed of a xenon lamp (150 W) and a monochromator (Omni-λ300) was focused and guided onto the ribbons. An oscilloscope (Tektronix, TDS2012B) and a mechanical light chopper (SRS, SR540) were utilized to investigate the time-resolved photoresponse of the devices.

3. Results and discussion

3.1. Morphological and structural characterization

Experimental setup and strategy for synthesis of ZnS/SnO_2 core/shell ribbons are illustrated in Scheme S1.† Briefly, we first synthesized ZnS ribbons *via* a H_2 assisted thermal evaporation process in a tube furnace (eqn (1) and (2)), as reported by our group previously.[28] Typical SEM images of the as-grown ZnS ribbons are exhibited in Fig. S1.† It can be seen (Fig. S1a, b†) that the Si substrate is fully covered by ZnS structures with lengths ranging from several tens to several hundreds of micrometers and widths up to several micrometers. Close observations (Fig. S1c, d†) further reveal that each ZnS microstructure presents a well-defined ribbon geometry with relatively smooth surfaces. Thickness of the ribbon was observed to be several tens of nanometers typically. TEM was also employed to probe the structure of the ZnS ribbons. Fig. S1e† shows a HRTEM image of the ZnS ribbon. The lattice fringes of wurtzite ZnS (0001) and (01−10) with *d*-spacings of 0.63 and 0.28 nm can be clearly resolved. The corresponding SAED pattern (Fig. S1f†) exhibits a set of well-arranged spots, which demonstrates that the synthesized ZnS ribbon is a single crystal.

Next, with our goal of achieving ZnS/SnO_2 core/shell heterojunctions, deposition of SnO_2 nanoparticles was carried out by using the ZnS ribbons as template and SnO powder as source material through a thermal disproportionation reaction (eqn (3)). It is worth mentioning that a temperature of 600 °C was set in the deposition area to avoid the deposition of Sn on the ZnS ribbons, and at the same time to achieve highly crystallized SnO_2 nanoparticles. Detailed procedures can be found in the Experimental section. Fig. 1a–c show representative SEM images of the final product at different magnifications, corresponding one-to-one with Fig. S1a–c† (SEM images of ZnS ribbons), respectively. It seems that no obvious change occurred according to the low-magnification SEM observations: the morphology of the product is retained afterwards and still exhibits a well-defined ribbon structure. However, the high-magnification SEM image shown in Fig. 1d clearly reveals that the surface of ribbon became significantly rougher in comparison to that of primary ZnS ribbon (Fig. 1e), suggesting a possibility that SnO_2 is coated on the ZnS ribbon. EDX analysis was also performed on the sample. As shown in Fig. S2,† the presence of Sn and O elements in the final product solidly

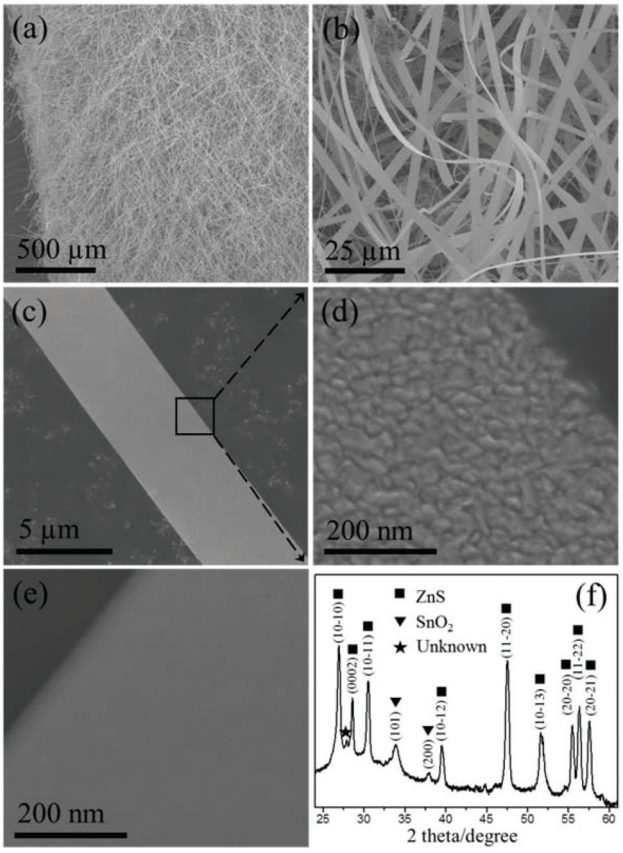

Fig. 1 (a–d) SEM images of ZnS/SnO_2 core/shell ribbons at different magnifications. (e) SEM image of a ZnS ribbon, showing a relatively smooth surface. (f) XRD pattern of the ZnS/SnO_2 core/shell ribbons with *y*-axis on a log scale.

demonstrates the successful deposition of SnO_2 on ZnS ribbon. In order to investigate the phase structure of SnO_2 nanoparticles, XRD measurement was carried out. Fig. 1f shows the XRD pattern of the as-synthesized ZnS/SnO_2 heterojunction ribbons, in which a biphase mixture of ZnS and SnO_2 was identifiable. In addition to those reflection peaks from the wurtzite ZnS[40] (JCPDS, no. 36-1450), the relatively weak peaks located at about 34° and 38° can be indexed to the (101) and (200) planes of rutile SnO_2[41] with lattice constants of a = 0.47 nm and c = 0.32 nm (JCPDS, no. 41-1445). Interestingly, it is also found that the intensity ratio between (101) and (200) reflections in the current study is much higher compared with that calculated from the standard XRD spectrum of polycrystalline SnO_2, indicating that there exists preferred crystallographic orientation for SnO_2 nanoparticles on ZnS ribbons.

$$ZnS + H_2 \xrightarrow{1100\,^{\circ}C} Zn + H_2S \quad (1)$$

$$Zn + H_2S \rightarrow ZnS + H_2 \quad (2)$$

$$2SnO \xrightarrow{850\,^{\circ}C} SnO_2 + Sn \quad (3)$$

To further verify the composition of the heterostructures, an elemental analysis was also carried out with EDX in scan-

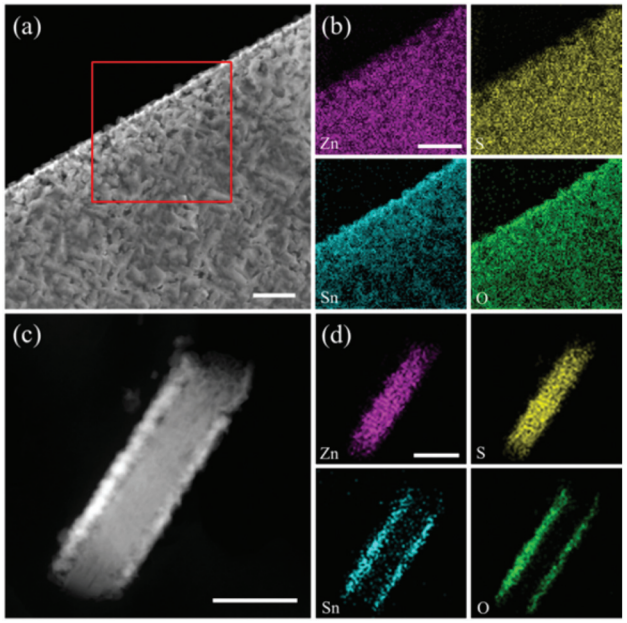

Fig. 2 (a, b) Plan-view and (c, d) cross-sectional view HAADF-STEM images and corresponding EDX elemental mapping of the ZnS/SnO_2 core/shell ribbons. Scale bar = 100 nm.

ning TEM (STEM) mode. Fig. 2a shows a plan-view high-angle annular dark field STEM (HAADF-STEM) image of a ribbon after the coating process. It can be seen that the surface of the ribbon is a little rugged, which is in good accordance with the SEM observation. The elemental mapping of the ribbon indicates that the rugged layer is SnO_2, which covers the surface of the ZnS ribbon. To give more insight into the constitution and chemical composition of heterostructures, cross-sections of ribbons were also prepared and, correspondingly, the EDX mapping was done as well. Fig. 2c is an HAADF image of the cross-section. It is known that in HAADF imaging mode, the intensity of the image scales with the square of atomic number Z. With a larger atomic number, SnO_2 would be brighter than ZnS in the image. In this regard, we can assign the outside layers with a relatively brighter contrast to the SnO_2, and the inner part to the ZnS. This is confirmed further by the relevant elemental mapping. As shown in Fig. 2d, the Zn and S elements distribute only in the center of the "sandwich" while Sn and O elements are detected exclusively in the two outer layers.

In order to investigate the structure of the ZnS/SnO_2 core/shell ribbon, TEM and SAED characterizations were carried out. Fig. 3a shows a low-magnification TEM image of the resultant heterostructure. It can be observed that SnO_2 nanoparticles, with typical diameters of about 15–35 nm, are homogenously and compactly covering the surface of the ZnS ribbon. The corresponding SAED pattern (Fig. 3b) reveals a superposition of two different sets of diffraction spots. One set represents well-orientated spots that can be assigned to [2−1−10] zone axis of wurtzite ZnS and the other set, with diffraction pattern composed of rings, can be assigned to

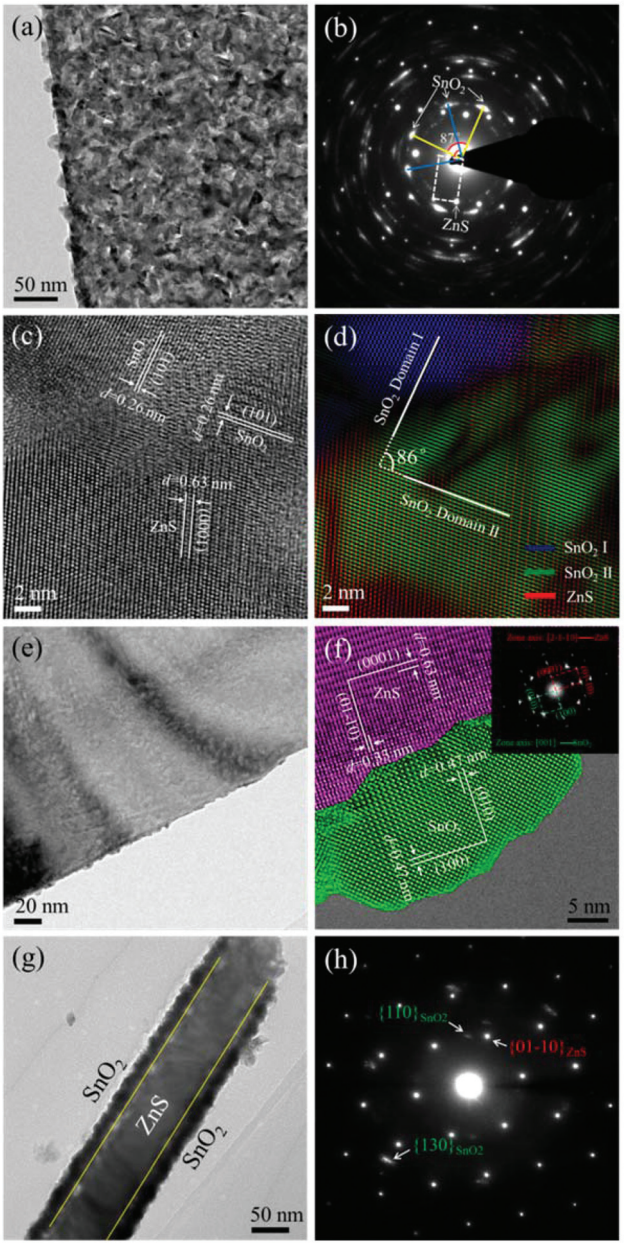

Fig. 3 (a) TEM image and (b) corresponding SAED pattern of ZnS/SnO_2 core/shell ribbon. (c) HRTEM image and (d) corresponding IFFT image, showing structure of ZnS and SnO_2, and their orientation relationship. (e) TEM image and (f) HRTEM image of ZnS/SnO_2 core/shell ribbon with low loading amount of SnO_2, showing the epitaxial relationship between the side surface of ZnS and the decorated SnO_2. (g) TEM image and (h) corresponding SAED pattern of cross-section of ZnS/SnO_2 core/shell ribbon.

rutile SnO_2. It is noteworthy that the intensities of (101) diffraction spots of SnO_2 are significantly enhanced, which indicates that the majority of SnO_2 nanoparticles have preferred orientations on the ZnS ribbon. This can be confirmed nicely by HAADF-STEM imaging of core/shell ribbon, as shown in Fig. S3a and b.† Interestingly, those particles have an equivalent zone axis after analysis, *i.e.*, <−313> of rutile SnO_2

(Fig. S3c–e).† Fig. 3c shows an HRTEM image of the ZnS/SnO_2 heterostructured ribbon, in which the lattice fringes of the wurtzite ZnS (0001) and rutile SnO_2 (101), with *d*-spacings of 0.63 nm and 0.26 nm, are revealed. The angle between the (101) planes of two SnO_2 particles is measured as 86°, well consistent with that of (101) electron diffractions of SnO_2, as indicated in Fig. 3b. Fig. 3d is a constructed inverse fast Fourier transform (IFFT) image extracted from the image of Fig. 3c. It is very clear now that the two SnO_2 particle domains, orientated with their (101) planes with an angle of 86°, are located on the (2–1–10) facet of the ZnS ribbon. Fig. 3a shows a low-magnification TEM image of heterostructured ribbon with a low coating density of SnO_2. As observed, only a few SnO_2 nanoparticles are found to be decorated on the side facets of the ribbon. The low coating density enables us to directly resolve the fine structure of hetero-interface. Fig. 3f and Fig. S4a–d† show representative HRTEM images taken from the interfacial region between SnO_2 nanoparticles and side facets of ZnS ribbon. It is interesting to note that the two components exhibit exactly the same orientation relationship in all cases, which is given by $(01\text{–}10)_{ZnO}//(020)_{SnO_2}$ and $[2\text{–}1\text{–}10]_{ZnO}//[001]_{SnO_2}$. Fig. 3g is a cross-sectional image of sandwiched ribbon. As demonstrated already by EDX mapping, the central part is ZnS and the shells are SnO_2. Their thicknesses are measured to be ~80 nm and ~20 nm, respectively. Fig. 3h is the corresponding SAED pattern of the "sandwich", in which a superposition composed of two different sets of diffraction spots was identifiable. The hexagonally arranged spots are from the [0001] zone axis of wurtzite ZnS while the other set of sporadic spots can be assigned to rutile SnO_2, as indicated in the image. HRTEM image of the ZnS/SnO_2 cross section and relevant reconstructed image are displayed in Fig. S5 in the ESI.†

3.2. Electronic and optoelectronic properties

With high crystallinity, large surface-to-volume ratio and unique physical and chemical properties of the constituent materials, ZnS/SnO_2 core/shell heterostructured ribbons may be promising candidates for efficient electronic and optoelectronic applications. To examine electrical transport properties of the product, nano-back-gate FETs based on ZnS/SnO_2 core/shell heterostructures were assembled by standard photolithography and lift-off processes. Details of device fabrication can be found in the Experimental section. As illustrated schematically in Fig. 4a and from the SEM image shown in the inset of Fig. 4b, devices were made by depositing a pair of indium tin oxide (ITO) electrodes with an interval of 15 μm on ZnS/SnO_2 core/shell ribbons. To optimize the electrode materials for this system, Au electrodes were also chosen in this work. In the case of ZnS ribbon, its conductivity is generally very low due to the low concentration of free carriers. As shown in Fig. 4b, the ZnS ribbon gives a low dark current with noise level, that is, $\sim 10^{-13}$ A at V_{ds} = 5 V. After coating of a SnO_2 layer, the formed ZnS/SnO_2 heterostructure is expected to have a larger current due to the relatively high conductivity of SnO_2.[33] It was measured that under the Au contact, ZnS/SnO_2

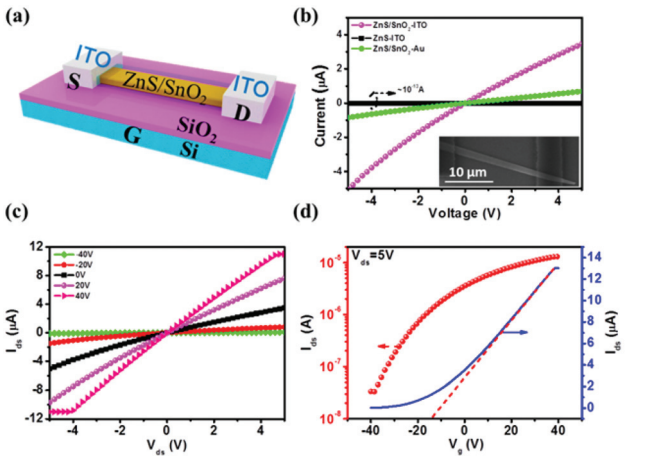

Fig. 4 (a) Schematic diagram of a device for the electrical measurement. (b) Typical *I*–*V* curves of a single ZnS/SnO_2 ribbon and ZnS ribbon by using ITO and Au as source and drain electrode, respectively; inset is an SEM image of the device. (c) I_{ds}–V_{ds} curves plotted at various V_g. (d) I_{ds}–V_g curve at V_{ds} = 5 V.

ribbon shows a significantly enhanced current of ~0.7 μA at V_{ds} = 5 V. This value is about 6 orders of magnitude higher than that of ZnS ribbon. However, the largest conduction current was recorded by using the ITO electrodes, that is, 3.5 μA at V_{ds} = 5 V. This result indicates that the ITO electrodes have better contacts with the heterostructured ribbon, which are more suitable for the ZnS/SnO_2 heterostructure-based FETs. Especially after the annealing process, indium in the ITO may diffuse across the interface, leading to a decrease in the contact barrier and a boost to electron tunneling transport by thermionic or thermionic-field emission.

Fig. 4c shows source-drain current (I_{ds}) as a function of source-drain voltage (V_{ds}) recorded at diverse gate voltages (V_g). It is seen that the current increases with the change of gate voltage from −40 V to +40 V, presenting a typical n-type semiconductor characteristic. The I_{ds} reaches ~11 μA at a V_g of +40 V, and is turned off when V_g is lower than −40 V. Fig. 4d shows the I_{ds} *versus* V_g plot of the device measured at a V_{ds} of 5 V. It is noteworthy that the device can give a large I_{ON}/I_{OFF} ratio of over 10^3, suggesting a good modulation ability of the gate voltage to the channel conduction. According to the relationship of $g_m = dI_{ds}/dV_g$, the transconductance (g_m) of the FET is deduced to be ~265 nS in the linear regime of the I_{ds}–V_g curve. This value was employed to calculate the carrier mobility μ_n and concentration n_e according to the following equations:

$$g_m = dI_{ds}/dV_g = Z\mu_n C_0 V_{ds}/L \quad (4)$$

$$n_e = \sigma/q\mu_n \quad (5)$$

wherein C_0 is the gate oxide capacitance per unit area, Z (2.5 μm) is the width of the channel, L (18 μm) is the length of the channel, and σ is the conductivity of the heterostructured ribbon at V_g = 0 V. Knowing that the SiO_2 dielectric constant is around 3.9 and its thickness is about 300 nm in our case, the gate capacitance C_0 is calculated to be 1.15×10^{-8} F cm^{-2}.

From these values, the field-effect carrier mobility μ_n and concentration n_e are estimated to be 33.2 $cm^2\ V^{-1}\ s^{-1}$ and 7.9 × $10^{16}\ cm^{-3}$, respectively. The high electron mobility of the ZnS/SnO_2 core/shell heterojunction shows promising potential for efficient electronics.

Optoelectronic properties of the ZnS/SnO_2 core/shell heterostructure were also investigated. Fig. 5a shows the current–voltage (I–V) curves of an individual ZnS/SnO_2 core/shell ribbon under monochromatic light of different wavelengths. It is evident that the current of the device depends strongly on the wavelength of light. When the device was illuminated with 320 nm UV light at 0.1 mW cm^{-2}, the current across the device can reach 17.4 μA at an applied voltage of 5 V. However, illumination of 550 nm light on the device only gives a low current of 3.6 μA (almost the dark current level, 3.5 μA), indicating a visible-blind characteristic. It is also noted that the I–V curves are symmetrical about the origin and exhibit linearly dependent characteristic, indicating a good Ohmic contact between the ribbon and the ITO electrodes.[16] Fig. 5b shows the spectroscopic photoresponse of the device as a function of the incident light wavelength at a bias voltage of 1 V. The cut-off wavelength of the device is shown to be ~370 nm and light with energy below this threshold wavelength is insufficient to generate electron–hole pairs in the ribbon. When the device was illuminated by light with energy above this threshold wavelength, the photoresponse exhibited a significant increase by about four to six orders of magnitude, demonstrating that our device is suitable as a visible-blind UV photodetector. The increase step at an excitation energy range from 3.35 eV to 3.87 eV (corresponding to 320–370 nm wavelength range) is close to the bandgap energies of SnO_2 (3.6 eV) and ZnS (3.77 eV), respectively. Fig. 5c depicts a time-dependent response of the device by switching light illumination (320 nm, ~0.1 mW cm^{-2}) on and off periodically at a fixed voltage of 1.0 V. The device shows a good stability and reproducibility: upon UV illumination, the photocurrent increased to a stable value of ~3.2 μA, and then dropped down to the initial value of ~0.4 μA when the light was turned off, with a photocurrent to dark current ratio (I_{light}/I_{dark}) of ~8. This ratio can be increased with an elevated light intensity. The photoconductive mechanism in the ZnS/SnO_2 core/shell ribbon can be understood by processes of adsorption and desorption of oxygen molecules on the ribbon, similar to those reported previously in other semiconductors.[17,42] In ambient conduction, the oxygen molecules are adsorbed on the surface of the ribbon and trap the free electrons in the form of [$O_2 + e^- \rightarrow O_2^-$], creating a low-conductivity depletion layer near the surface. When the device is illuminated with UV light, electron–hole pairs are generated as a consequence, which would migrate to the surface of the ribbon and desorb the oxygen *via* the reaction [$O_2^- + h^+ \rightarrow O_2$]. This process decreases the thickness of the depletion layer and increases the concentration of free carriers, leading to a significantly enhanced photocurrent as a consequence.

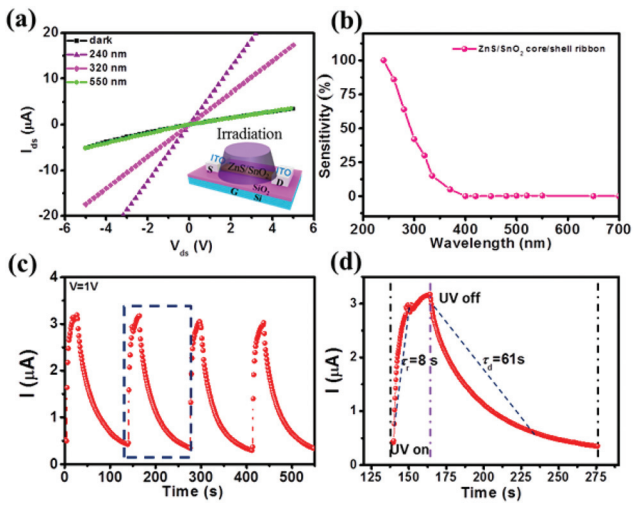

Fig. 5 (a) I–V curves of the device illuminated under various wavelengths. (b) Spectral response of the device at various wavelengths under V_{ds} = + 1.0 V. The constant light intensity is 0.1 mW cm^{-2}. (c) Time-resolved photoresponse of the device under V_{ds} = + 1.0 V. (d) Enlarged 135–280 s range of photoresponse to evaluate rise time (τ_r) and decay time (τ_d) of the device.

In addition to stability and reproducibility, the response speed is also an important parameter to evaluate the performance of a photodetector. The time accounting for the photocurrent increasing from 10% to 90% of peak value or *vice versa* is defined as the rise time and decay time, respectively. According to the photoresponse of the device shown in Fig. 5d, the rise time and decay time are determined to be ~8 s and ~61 s, respectively. Although the values are not as good as those for devices made of intrinsic ZnS nanoribbons, they are better than those for photodetectors fabricated with n-doped ZnS nanostructures, such as ZnS : Al and ZnS : Cl nanowires.[43,44] It is also worth mentioning that our device shows the ability to work under pulsed UV irradiation. Fig. 6a and b present photoresponse of the device at a chopper frequency of 10 Hz and 150 Hz, respectively. The distinct on/off state indicates that the device can well follow pulsed UV irradiation with various chopper frequencies. Fig. 6c plots the relative balance ($I_{max} - I_{min}$)/I_{max} as a function of switching frequency of the device. Although the relative balance value decrease gradually with an increase of frequency, the device still retains a relative balance of about 45% at a high frequency of f = 200 Hz, suggesting a promising potential of the device to monitor ultrafast UV light signals.

The spectral responsivity (R) defined as the photocurrent generated per unit power of incident light on the effective area of a photoconductor and the external quantum efficiency (EQE) related to the number of electron–hole pairs excited by one absorbed photon are key parameters to determine the sensitivity of a photodetector.[16] Based on eqn (6) and (7), R and EQE values of the device are calculated to be ~6.2 × 10^4 A W^{-1} and ~2.4 × 10^7%, respectively, at V_{ds} = +1 V, where I_p is the photocurrent, P_{opt} is the incident light intensity, S is the effective illuminated area, h is Planck's constant, c is the velocity of light, q is the electronic charge, and λ is the incident light wavelength. Such high R and EQE values demonstrate an

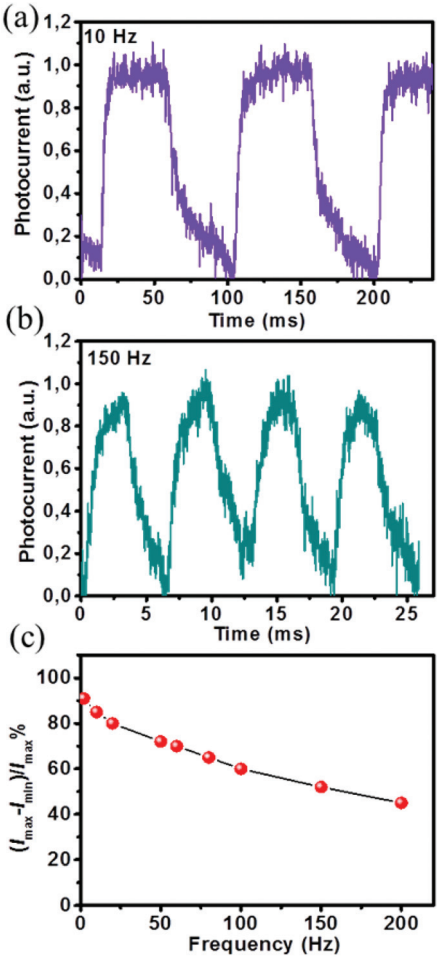

Fig. 6 Response characteristics of the device to pulsed UV light (320 nm, 0.1 mW cm^{-2}) at chopper frequency of (a) 10 Hz and (b) 150 Hz. (c) The relative balance $(I_{max} - I_{min})/I_{max}$ *versus* switching frequency.

excellent photosensitivity of the ZnS/SnO_2 heterojunction-based photodetector.

$$R(\mathrm{A\,W^{-1}}) = \frac{I_p}{P_{opt}S} \quad (6)$$

$$\mathrm{EQE} = \frac{hc}{q\lambda}R \quad (7)$$

We propose that the high photocurrent and photosensitivity in the present device may relate to the prolonged photocarrier lifetime by spatial separation of the photogenerated electron–hole pairs, considered to be attributed to the type-II band alignment of the ZnS and SnO_2. Owing to the formation of an internal field at the ZnS/SnO_2 heterointerface, the photogenerated electrons will move to the SnO_2 side with concomitant transfer of photogenerated holes to the ZnS side, forming a spatial charge separation state within the core/shell ribbon (Fig. S6†). This charge separation state can effectively decrease the recombination of the electron–hole pairs,[8,39,45,46] and thus can markedly increase the photocurrent and the external quantum efficiency of the device. Similar phenomenon has been observed in the case of a ZnO/ZnS biaxial nanoribbon-based photodetector.[16] Besides, high crystallinity and relatively fast carrier mobility, as well as good Ohmic contact between ZnS/SnO_2 core/shell ribbon and ITO electrodes are also considered to be beneficial for obtaining a high photocurrent. Summarized in Table 1 are the main characteristic parameters of the ZnS/SnO_2 heterostructured ribbon-based photodetector in the present study, and photodetectors made of ZnS nanoribbons and SnO_2 nanowires from previous reports, for comparison. One can see that the current ZnS/SnO_2-based photodetector exhibits advantages of fast electron mobility, large photocurrent, high EQE and relatively fast response time, which in general go beyond those of most other devices for optoelectronic applications. Especially when comparing the photodetector from doped ZnS nanowires, our device not only shows comparable photocurrent and EQE values, but also shows much faster carrier mobility and response speed. Moreover, it is also worth mentioning that unlike the synthesis of doped ZnS that generally involves complex and uncontrollable doping process, fabrication of ZnS/SnO_2 heterostructures herein is straightforward and controllable. To sum up, our results demonstrate that the as-prepared type-II ZnS/SnO_2 core/shell heterostructure could be used for effective UV light sensing, and more importantly, has the advantages of type-II semiconducting heterostructures for construction of high-performance nano-photodetectors.

4. Conclusion

In summary, we report a simple two-step thermal evaporation approach to synthesize ZnS/SnO_2 core/shell heterostructured ribbons for the first time. The heterostructure consists of SnO_2 nanoparticles with sizes of about 15–35 nm that uniformly and compactly cover the surface of the ZnS ribbon as a continuous layer. Structural analysis indicated that most SnO_2 nanoparticles have preferred orientation relationships with the ZnS ribbon. Particularly, SnO_2 nanoparticles were shown to

Table 1 Comparison of characteristic parameters of ZnS/SnO_2 core/shell ribbon-based UV photodetector, and ZnS and SnO_2 nanostructure-based UV photodetectors

Photoconductors	Mobility ($cm^2\ V^{-1}\ s^{-1}$)	Dark current	Photocurrent	EQE/gain (%)	Response time (τ_r, τ_f)	Reference
ZnS nanoribbons	—	<1 pA (5 V)	1 pA (5 V)	50	<0.3 s, <0.3 s	25
SnO_2 nanowires	—	40 nA (0.1 V)	200 nA (0.1 V)	8×10^5	—, >100 s	29
ZnS : Al nanowires	0.16	<0.2 μA (5 V)	<1.5 μA (5 V)	4.3×10^8	95 s, 209 s	44
ZnS/SnO_2 core/shell ribbon	33.2	0.4 μA (1 V)	3.2 μA (1 V)	2.4×10^7	8 s, 61 s	This work

grow epitaxially on the side surfaces of the ZnS ribbon with orientation relationships of $(01-10)_{ZnO}//(020)_{SnO_2}$ and $[2-1-10]_{ZnO}//[001]_{SnO_2}$. Electrical property study of the synthesized ZnS/SnO_2 core/shell heterostructure was carried out by constructing a FET, which exhibits a high on/off ratio of $\sim 10^3$ and a high mobility of ~ 33.2 cm^2 V^{-1} s^{-1}. Moreover, the optoelectronic properties of the sample were also investigated, which showed good operating performances, including large photocurrent, high sensitivity (high R and EQE values), good stability and reproducibility, and relatively fast response speed. Our results indicate that the as-synthesized ZnS/SnO_2 core/shell heterostructured ribbons could be promising candidates for high-performance UV-light detection. Last but not least, it is also expected that our approach could be extended to fabricate other functional core/shell heterostructures, such as ZnO/SnO_2, TiO_2/SnO_2, and Si/SnO_2.

Acknowledgements

The authors would like to thank the "Strategic Priority Research Program" of the Chinese Academy of Sciences (XDA09040203) and 973 Project (2012CB932401) for the financial support. X. Huang also would like to thank the "Doctoral Training Programme" of Max-Planck Society and Chinese Academy of Sciences. X. Huang and Y. Q. Yu contributed equally to this work.

Notes and references

1 L. F. Hu, M. M. Brewster, X. J. Xu, C. C. Tang, S. Gradecak and X. S. Fang, *Nano Lett.*, 2013, **13**, 1941–1947.
2 J. Xiang, W. Lu, Y. J. Hu, Y. Wu, H. Yan and C. M. Lieber, *Nature*, 2006, **441**, 489–493.
3 X. P. Qi, G. W. She, X. Huang, T. P. Zhang, H. M. Wang, L. X. Mu and W. S. Shi, *Nanoscale*, 2014, **6**, 3182–3189.
4 Y. J. Hwang, A. Boukai and P. D. Yang, *Nano Lett.*, 2009, **9**, 410–415.
5 F. Zhang, S. M. Niu, W. X. Guo, G. Zhu, Y. Liu, X. L. Zhang and Z. L. Wang, *ACS Nano*, 2013, **7**, 4537–4544.
6 X. Huang, M. Wang, M. G. Willinger, L. D. Shao, D. S. Su and X. M. Meng, *ACS Nano*, 2012, **6**, 7333–7339.
7 J. Y. Xu, L. Ma, P. F. Guo, X. J. Zhuang, X. L. Zhu, W. Hu, X. F. Duan and A. L. Pan, *J. Am. Chem. Soc.*, 2012, **134**, 12394–12397.
8 H. McDaniel, P. E. Heil, C. L. Tsai, K. Kim and M. Shim, *ACS Nano*, 2011, **5**, 7677–7683.
9 X. Huang, M. Wang, L. D. Shao, M. G. Willinger, C. S. Lee and X. M. Meng, *J. Phys. Chem. Lett.*, 2013, **4**, 740–744.
10 B. Kalisky, E. M. Spanton, H. Noad, J. R. Kirtley, K. C. Nowack, C. Bell, H. K. Sato, M. Hosoda, Y. W. Xie, Y. Hikita, C. Woltmann, G. Pfanzelt, R. Jany, C. Richter, H. Y. Hwang, J. Mannhart and K. A. Moler, *Nat. Mater.*, 2013, **12**, 1091–1095.
11 L. Ma, W. Hu, Q. L. Zhang, P. Y. Ren, X. J. Zhuang, H. Zhou, J. Y. Xu, H. L. Li, Z. P. Shan, X. X. Wang, L. Liao, H. Q. Xu and A. L. Pan, *Nano Lett.*, 2014, **14**, 694–698.
12 B. M. Nguyen, Y. Taur, S. T. Picraux and S. A. Dayeh, *Nano Lett.*, 2014, **14**, 585–591.
13 B. D. Liu, Y. Bando, B. Dierre, T. Sekiguchi, D. Golberg and X. Jiang, *ACS Appl. Mater. Interfaces*, 2013, **5**, 9199–9204.
14 W. Tian, C. Zhang, T. Y. Zhai, S. L. Li, X. Wang, J. W. Liu, X. Jie, D. Q. Liu, M. Y. Liao, Y. Koide, D. Golberg and Y. Bando, *Adv. Mater.*, 2014, **26**, 3088–3093.
15 J. Yan, X. S. Fang, L. D. Zhang, Y. Bando, U. K. Gautam, B. Dierre, T. Sekiguchi and D. Golberg, *Nano Lett.*, 2008, **8**, 2794–2799.
16 L. F. Hu, J. Yan, M. Y. Liao, H. J. Xiang, X. G. Gong, L. D. Zhang and X. S. Fang, *Adv. Mater.*, 2012, **24**, 2305–2309.
17 W. Tian, T. Y. Zhai, C. Zhang, S. L. Li, X. Wang, F. Liu, D. Q. Liu, X. K. Cai, K. Tsukagoshi, D. Golberg and Y. Bando, *Adv. Mater.*, 2013, **25**, 4625–4630.
18 D. V. Talapin, I. Mekis, S. Gotzinger, A. Kornowski, O. Benson and H. Weller, *J. Phys. Chem. B*, 2004, **108**, 18826–18831.
19 J. Schrier, D. O. Demchenko and L. W. Wang, *Nano Lett.*, 2007, **7**, 2377–2382.
20 Y. J. Guo, C. E. Rowland, R. D. Schaller and J. Vela, *ACS Nano*, 2014, **8**, 8334–8343.
21 B. C. Cheng, J. Xu, Z. Y. Ouyang, X. H. Su, Y. H. Xiao and S. J. Lei, *J. Mater. Chem. C*, 2014, **2**, 1808–1814.
22 K. Wang, J. J. Chen, Z. M. Zeng, J. Tarr, W. L. Zhou, Y. Zhang, Y. F. Yan, C. S. Jiang, J. Pern and A. Mascarenhas, *Appl. Phys. Lett.*, 2010, **96**, 123105.
23 H. Choi, J. G. Radich and P. V. Kamat, *J. Phys. Chem. C*, 2014, **118**, 206–213.
24 X. Huang, M. G. Willinger, H. Fan, Z. L. Xie, L. Wang, A. Klein-Hoffmann, F. Girgsdies, C. S. Lee and X. M. Meng, *Nanoscale*, 2014, **6**, 8787–8795.
25 X. S. Fang, Y. Bando, M. Y. Liao, U. K. Gautam, C. Y. Zhi, B. Dierre, B. D. Liu, T. Y. Zhai, T. Sekiguchi, Y. Koide and D. Golberg, *Adv. Mater.*, 2009, **21**, 2034–2039.
26 X. S. Fang, L. M. Wu and L. F. Hu, *Adv. Mater.*, 2011, **23**, 585–598.
27 Y. Jiang, X. M. Meng, J. Liu, Z. R. Hong, C. S. Lee and S. T. Lee, *Adv. Mater.*, 2003, **15**, 1195–1198.
28 Y. Jiang, X. M. Meng, J. Liu, Z. Y. Xie, C. S. Lee and S. T. Lee, *Adv. Mater.*, 2003, **15**, 323–327.
29 C. H. Lin, R. S. Chen, T. T. Chen, H. Y. Chen, Y. F. Chen, K. H. Chen and L. C. Chen, *Appl. Phys. Lett.*, 2008, **93**, 112115.
30 W. Tian, C. Zhang, T. Y. Zhai, S. L. Li, X. Wang, M. Y. Liao, K. Tsukagoshi, D. Golberg and Y. Bando, *Chem. Commun.*, 2013, **49**, 3739–3741.
31 X. L. Wang, N. Aroonyadet, Y. Z. Zhang, M. Meckenburg, X. Fang, H. T. Chen, E. Goo and C. W. Zhou, *Nano Lett.*, 2014, **14**, 3014–3022.

32 T. T. Zhuang, P. Yu, F. J. Fan, L. Wu, X. J. Liu and S. H. Yu, *Small*, 2014, **10**, 1394–1402.
33 C. Hao, H. Linfeng, F. Xiaosheng and W. Limin, *Adv. Funct. Mater.*, 2012, **22**, 130–136.
34 Q. Kuang, C. S. Lao, Z. L. Wang, Z. X. Xie and L. S. Zheng, *J. Am. Chem. Soc.*, 2007, **129**, 6070–6071.
35 C. Ma, D. Moore, J. Li and Z. L. Wang, *Adv. Mater.*, 2003, **15**, 228–231.
36 H. Liu, Z. M. Zhang, L. F. Hu, N. Gao, L. W. Sang, M. Y. Liao, R. Z. Ma, F. F. Xu and X. S. Fang, *Adv. Opt. Mater.*, 2014, **2**, 771–778.
37 L. F. Hu, J. Yan, M. Y. Liao, L. M. Wu and X. S. Fang, *Small*, 2011, **7**, 1012–1017.
38 D. Gross, I. Mora-Sero, T. Dittrich, A. Belaidi, C. Mauser, A. J. Houtepen, E. Da Como, A. L. Rogach and J. Feldmann, *J. Am. Chem. Soc.*, 2010, **132**, 5981–5983.
39 X. Huang, L. Shang, S. Chen, J. Xia, X. P. Qi, X. C. Wang, Z. T. R. Zhang and X. M. Meng, *Nanoscale*, 2013, **5**, 3828–3833.
40 Z. W. Wang, L. L. Daemen, Y. S. Zhao, C. S. Zha, R. T. Downs, X. D. Wang, Z. L. Wang and R. J. Hemley, *Nat. Mater.*, 2005, **4**, 922–927.
41 L. Gracia, A. Beltran and J. Andres, *J. Phys. Chem. B*, 2007, **111**, 6479–6485.
42 C. Soci, A. Zhang, B. Xiang, S. A. Dayeh, D. P. R. Aplin, J. Park, X. Y. Bao, Y. H. Lo and D. Wang, *Nano Lett.*, 2007, **7**, 1003–1009.
43 Y. Q. Yu, J. S. Jie, P. Jiang, L. Wang, C. Y. Wu, Q. Peng, X. W. Zhang, Z. Wang, C. Xie, D. Wu and Y. Jiang, *J. Mater. Chem.*, 2011, **21**, 12632–12638.
44 P. Jiang, J. S. Jie, Y. Q. Yu, Z. Wang, C. Xie, X. W. Zhang, C. Y. Wu, L. Wang, Z. F. Zhu and L. B. Luo, *J. Mater. Chem.*, 2012, **22**, 6856–6861.
45 S. Jeong, M. Choe, J. W. Kang, M. W. Kim, W. G. Jung, Y. C. Leem, J. Chun, B. J. Kim and S. J. Park, *ACS Appl. Mater. Interfaces*, 2014, **6**, 6170–6176.
46 J. Xu, X. Yang, H. K. Wang, X. Chen, C. Y. Luan, Z. X. Xu, Z. Z. Lu, V. A. L. Roy, W. J. Zhang and C. S. Lee, *Nano Lett.*, 2011, **11**, 4138–4143.